Detectable anthropogenic changes in daily-scale circulations driving summer rainfall shifts over eastern China

ENVIRONMENTAL RESEARCH
LETTERS

LETTER • OPEN ACCESS

Detectable anthropogenic changes in daily-scale circulations driving summer rainfall shifts over eastern China

ENVIRONMENTAL RESEARCH
LETTERS

LETTER

Detectable anthropogenic changes in daily-scale circulations driving summer rainfall shifts over eastern China

Baiquan Zhou[1], **Panmao Zhai**[1,*], **Simon F B Tett**[2] **and Fraser C Lott**[3]

[1] State Key Laboratory of Severe Weather, Chinese Academy of Meteorological Sciences, China Meteorological Administration, Beijing, People's Republic of China
[2] School of Geosciences, University of Edinburgh, Edinburgh, United Kingdom
[3] Met Office Hadley Centre, Met Office, Exeter, United Kingdom
[*] Author to whom any correspondence should be addressed.

E-mail: pmzhai@cma.gov.cn

Keywords: circulation pattern, southern flood–northern drought, anthropogenic influence, dynamic and thermodynamic contribution

Supplementary material for this article is available online

OPEN ACCESS

RECEIVED
12 April 2021

REVISED
21 June 2021

ACCEPTED FOR PUBLICATION
28 June 2021

PUBLISHED
12 July 2021

Abstract

Wetting in the south while drying in the north during the last few decades constitutes the well-known 'southern flood–northern drought' (SFND) precipitation pattern over eastern China. The fingerprint of anthropogenic influence on this dipole pattern of regional precipitation trends has not been confirmed, especially for forced changes in relevant dynamics at the synoptic scale. Using a process-based approach involving model experiments both with and without anthropogenic inputs, it is demonstrated that the occurrences of daily circulation patterns (CPs) governing precipitation over eastern China during 1961–2013 have been altered by human influence. Due to anthropogenic forcing, CPs favoring SFND have become more likely to occur at the expense of CPs unfavorable to SFND. Regression analysis shows that changes recorded in the occurrence of CPs from the factual simulations could explain a large part of the precipitation trends over eastern China. CP frequencies driven by purely natural forcing do not reproduce this dipole pattern nor the inferred magnitude of precipitation trends over eastern China. These results suggest that human influence has played a critical role in shaping the contrasting north–south precipitation trends.

1. Introduction

With growing concerns about the regional impacts of the expected increase in flood and drought frequency under global warming, understanding how precipitation responds to anthropogenic forcing in a particular region is becoming immensely important for informing local adaptation and mitigation planning (Field *et al* 2012, Sarojini *et al* 2016). Although the evidence for anthropogenically forced precipitation change on the global and continental scales continues to strengthen, attribution of regional changes in precipitation remains a huge challenge (Min *et al* 2008, Stott *et al* 2010, Hegerl and Zwiers 2011, Sarojini *et al* 2016). At the regional scale, changes in atmospheric circulation exert strong control on local climate, which could reinforce or counteract the response of regional precipitation to external forcing (Bindoff *et al* 2013, Shepherd 2014, Pfahl *et al* 2017). Strong spatial variation, large internal variability and model errors arise, thus precluding the detection of anthropogenic signals in precipitation change (Stott *et al* 2010, Hegerl and Zwiers 2011, Bindoff *et al* 2013, Ma *et al* 2017). However, it is believed that improved process understandings will provide greater opportunity for studies on the attribution of regional precipitation change (Sarojini *et al* 2016).

During the past few decades, eastern China's summers have become wetter in the south but drier in the north, and the region has witnessed the increasing exposure of agriculture, infrastructure and human life to the devastating damage caused by severe floods and droughts (Ding *et al* 2008, Huang *et al* 2013, Qian and Zhou 2014, Nigam *et al* 2016, Li and Lu 2017, Day *et al* 2018). This well-known 'southern flood–northern drought' (SFND) precipitation

pattern, associated mainly with the weakening East Asia summer monsoon (EASM), has therefore motivated multiple detection and attribution (D&A) studies (Zhou *et al* 2009, 2017). Previous studies, that focused on changes in the decadal-scale mean state of circulation and precipitation pattern related to the EASM, have detected impacts of anthropogenic forcing and internal variability on the SFND using climate model simulations (Wang *et al* 2013, Song *et al* 2014, Jiang *et al* 2017, Yang *et al* 2017, Tian *et al* 2018, Dong *et al* 2019). However, when examining trends in summer precipitation and confronting model simulations with observations, D&A results remain controversial and progress is confined to identifying detectable human influence on the changing distribution of precipitation in eastern China (Liu *et al* 2015, Burke and Stott 2017, Ma *et al* 2017, Lu *et al* 2020). More specifically, different climate models with imperfect simulations of precipitation trends give nearly opposite signal of changes in total summer precipitation over eastern China, which consequently lead to equivocal D&A conclusions (Burke and Stott 2017, Lu *et al* 2020). Therefore, uncertainty in model simulations of trends in summer precipitation over eastern China obscures the detectability of human influence (Zhang 2015, Lu *et al* 2020). Additionally, precipitation trends of the opposite sign offsetting each other induced by averaging simplistically over eastern China where north–south contrasting precipitation changes are located may be another barrier to disentangling anthropogenic signals (Zhang *et al* 2007).

Recent studies have sought to improve understanding of the dynamic and thermodynamic mechanisms behind the EASM response to external forcing using moisture budget analysis, while changes in precipitation and evaporation cannot be isolated (Li *et al* 2015, Zhou *et al* 2020b). Through tracking the occurrence of daily circulation patterns (CPs) using self-organizing map (SOM) cluster analysis, Zhou *et al* (2020a) demonstrated the changing prevalence of CPs is robust and can well explain SFND over eastern China. The dynamic effect stemming from changes in CPs along with the dynamic–thermodynamic interactions dictate the latitudinal boundary of SFND. The framework of combining the dynamic (related to atmospheric circulation) and thermodynamic (linked to temperature change) decomposition with targeted model experiments has shown some success in the attribution of continent-scale precipitation change and probabilistic event attribution (Marvel and Bonfils 2013, Schaller *et al* 2016, Vautard *et al* 2016) and is promising to shed light on the attribution of the contrasting precipitation trends over eastern China.

As noted above, the critical but poorly understood role of dynamic processes highlights the importance of identifying dynamic responses to external forcing, which could subsequently facilitate the D&A of regional precipitation changes (Corti *et al* 1999, Shepherd 2014, Sarojini *et al* 2016). Using a process-based approach, we build on the SOM cluster analysis in Zhou *et al* (2020a) to address whether anthropogenic forcing impacts the frequency of large-scale daily CPs. Based on the link between CPs and summer precipitation, we infer if anthropogenic influence is detectable on the SFND pattern.

2. Materials and method

For the attribution analysis, we used a pair of model ensembles from the latest Met Office HadGEM3-GA6-based attribution system at N216 resolution (0.56° × ∼0.83° horizontal resolution, HadGEM3-A-N216 hereafter; Christidis *et al* 2013, Ciavarella *et al* 2018). One of these simulates the 'actual' world with both anthropogenic and natural (ALL) forcing and the other represents a counterfactual 'natural' world with only natural (NAT) forcing. Boundary conditions for ALL forcing are given by the observed sea surface temperatures (SSTs) and sea ice (SIC) fields from HadSST1 (Rayner *et al* 2003). For NAT forcing, the anthropogenically induced pattern of SSTs is removed from the observed SSTs. This is calculated as the multi-model mean difference between simulations with and without anthropogenic influence from the CMIP5 ensemble (Taylor *et al* 2012). Sea ice fields are also adjusted for the NAT forcing using an empirical relationship between historically observed polar SSTs and SIC (Christidis *et al* 2013, Ciavarella *et al* 2018). Each ensemble comprises 15 members during 1961–2013. As reflected in the more realistic precipitation globally and regionally benefited from high-resolution and forcing from prescribed SST and SIC, HadGEM3-A-N216 well captures many ongoing large-scale modes of variability (e.g. the El Niño–Southern Oscillation) and monsoon systems (Johnson *et al* 2016, Burke and Stott 2017, Ciavarella *et al* 2018, Li *et al* 2018). It also reproduces well the main large-scale CPs associated with local climate over Europe and their frequencies (Vautard *et al* 2019), as well as characteristics of circulation related to East Asian winter monsoon (Hao *et al* 2019). Despite the lack of ocean coupling, atmospheric general circulation models possess comparable skill to the coupled ones in simulating anthropogenic climate change and specifically the monsoon climatology over East Asia (He and Soden 2016, Li and Ting 2017). These aspects all support the utilization of HadGEM3-A-N216 to understand the large-scale dynamic responses to anthropogenic climate change.

The 20 CPs obtained from the SOM analysis (described later in this section) by Zhou *et al* (2020a), considered here as the reference circulation types for model simulations, were based on the reanalysis

product (ERA reanalysis hereafter) from a combination of ERA-40 covering 1961–1978 and ERA-Interim spanning 1979–2015, at a spatial resolution of 2° (Uppala *et al* 2005, Dee *et al* 2011). The concatenated ERA reanalysis has been widely used in atmospheric circulation typing and validated against other reanalysis datasets (Bao and Wallace 2015, Huguenin *et al* 2020, Zhou *et al* 2020a). Though not as high resolution as the latest ERA5 reanalysis dataset, the ERA reanalysis is demonstrated to be sufficient in resolving and discriminating the characteristics of various CPs as atmospheric circulation is characterized by large spatial scales (Boé and Terray 2008, Belleflamme *et al* 2013, Bao and Wallace 2015, Hersbach *et al* 2018, Huguenin *et al* 2020). Additionally, the computational cost of SOM is greatly reduced with a smaller size of input elements using the coarse resolution dataset (Tymvios *et al* 2010, Lennard and Hegerl 2015). We also used the observed daily precipitation data for the period 1961–2015 from 519 stations over eastern China (112°–121° E, 26°–42° N, red rectangle in figure S1 (available online at stacks.iop.org/ERL/16/074044/mmedia)) from the National Meteorological Information Center, China Meteorological Administration.

SOM consists of a two-dimensional array of nodes, each of which is represented by a reference vector equal in dimension to the input data sample (Kohonen 2001, Hewitson and Crane 2002). After initialization with random values, the reference vectors of the 'winning' node with the minimum Euclidean distance to the input vector and its surrounding nodes are updated to better resemble the input data space in an iterative training process. A two-phase training process, involving a first broad capture of the large-scale structure in the input data and a further fine-tuning of the nodes to obtain final convergence, has been demonstrated to allow for better separation between clusters (Jiang *et al* 2015, Lennard and Hegerl 2015). A 5 × 4 SOM containing 20 CPs was produced using the two-phase approach with the daily circulations represented by the temporally standardized anomalies of 500 hPa geopotential height (covering 30°–160° E, 10°−70° N) and mean sea level pressure (covering 105°–135° E, 15°–45° N) in summers during 1961–2015 from ERA reanalysis (figure S1; see also Zhou *et al* 2020a). The effect of thermal expansion on geopotential height related to global warming is not accounted for here. As discussed in Horton *et al* (2015) and Zhou *et al* (2020a), substantial regional variations in the direction and magnitude of the trends in 500 hPa geopotential heights suggest the inappropriateness of detrending either with the removal of uniform domain average trend (commonly used in previous clustering studies which assume uniform thermal dilation, Cattiaux *et al* 2013) or the removal of local geopotential height trends (the signal of changes in CPs would also be removed). Moreover, the same SOM analysis using the detrended geopotential heights with domain average linear trend removed from each grid has demonstrated no significant impact on the sign and magnitude of trends in CP occurences (Zhou *et al* 2020a).

The daily circulation fields from reanalysis and model simulations with and without anthropogenic forcing are projected onto the SOM and ascribed to the single best matching node (CP) according to pattern similarity measured by the Euclidean distance (Huth 2000, Belleflamme *et al* 2013, Rousi *et al* 2021), which easily allows characterization of the occurrence frequency of each CP (Reusch *et al* 2005, 2007). Simulations from HadGEM3-A-N216 are interpolated to the 2° × 2° grid of the ERA reanalysis prior to CP classification. CP frequencies in the HadGEM3-A-N216 simulations are scaled up by 92/90 as model months are 30 d giving 90 summer days. To measure the possible influence of resolution on clustering and the robustness of the clusters in the model simulations, the variance ratio defined as the ratio of the average inter-cluster squared distance to the mean intra-cluster variance is used (Fabiano *et al* 2020, Rousi *et al* 2021), which is calculated as:

$$R_{\mathrm{v}} = \frac{2 \times \sum_{C_{mn}} |C_m - C_n|^2}{(k-1) \times \sum_m {\sigma_m}^2}$$

where the summation in the numerator is done without repetition over all combinations of the clusters, k is the number of clusters and ${\sigma_m}^2$ is the intra-cluster variance. C_m and C_n are the respective cluster centroids represented here by the composite mean of daily circulations assigned to that node. Larger variance ratio indicates better separation between clusters with stronger intra-type compactness. As projecting daily circulation simulations with the original high resolution to the SOM derived from coarse resolution data is not practical, we assume for the same day the high-resolution circulation could be classified to the same type as the low-resolution one has been assigned to. We compare the variance ratios for the clusters derived from model simulations before and after interpolation to validate the above assumption and examine the influence of resolution on CP classification. If the more detailed circulation information brought from high-resolution simulations lowers the variance ratio a lot, it means the high-resolution simulations are much less clustered and the CP typing is sensitive to resolution. Nevertheless, for the multimember simulations from HadGEM3-A-N216, variance ratios show very slight decrease in the high-resolution clusters, which demonstrates that the resolution has indiscernible effect on the clustering of CPs (figure S2). Moreover, the comparable variance ratios between clusters from ERA reanalysis and the ALL forcing ensemble show that the clustering of CPs in the model simulations is as robust as that in the reanalysis (figure S2).

The linkage between the frequency changes in CPs and the precipitation response over eastern China are investigated through the composite observational precipitation anomalies calculated by averaging over the same days as those assigned to each CP. Considering the north–south dipole pattern of precipitation trends over eastern China (divided by 34° N), CPs are identified as neutral, wet and dry types for the north and south respectively, when the domain-averaged composite precipitation anomalies under each CP is within $\pm 0.5\sigma$, exceeding $+0.5\sigma$ and below -0.5σ (σ is the standard deviation of domain-averaged precipitation during 1961–2010; figure S3). Assuming the composite precipitation anomaly under each CP is temporally invariant, the dynamic contribution to trends in summer total precipitation anomalies can be calculated as the product of the composite precipitation anomaly and trends in the frequency of CPs (Horton *et al* 2015, Zhou *et al* 2020a). Our analyses focus on this dynamically induced precipitation change, which gives the precipitation trends purely due to changes in CP occurrence.

Risk ratio (RR)—a widely used metric in probabilistic event attribution calculated as the ratio between the two probability estimates in the ALL and NAT forcing ($RR = P(ALL)/P(NAT)$)—is used here to measure the likelihood of human-induced changes (Stott *et al* 2016). By fitting probability density functions (PDFs) to the histogram of the variable considered, the probability of an event defined by the variable exceeding (or not exceeding) a prespecified threshold is calculated as the area under the PDF curve above (below) this threshold. All of the fitted PDFs are derived from a rectangular kernel density estimation, which applies weak smoothing and retains most of the information in the PDFs estimated from histograms (Fischer *et al* 2013). Unlike a histogram, which estimates PDF by assigning equal density value to every data point within discrete bins, the kernel density estimation fits individual probability density curve for each data value and then sums all these small PDFs together to obtain a smooth and continuous PDF curve. Prior to fitting PDFs, frequencies of CPs in both ERA reanalysis and each member from model simulations are normalized by their respective means and inter-annual standard deviations obtained from 1961 to 2010 for robust comparison between them. The NAT forcing simulations are normalized using the same statistics from ALL forcing experiment. The 95% CI is derived from the 1000 times resampling using bootstrapping (Efron and Tibshirani 1998). Each bootstrap creates a set of new data with the same length as the original by randomly resampling with replacement. Statistics of interest such as RR, return period and the corresponding threshold are computed 1000 times via the PDFs generated from the 1000 resamples. The 2.5th and 97.5th percentiles are then used to indicate the 95% CI.

3. Results

On the topologically ordered SOM plane, similar CPs are mapped onto adjacent nodes, while very distinct CPs are placed far apart (figure S1). The 20 CPs are named with the combination of column label denoted by capital letters (A to D) and the row label indicated by numbers (1–5). Patterns A1 and A2 in the top-left feature intense and westward extended western Pacific subtropical high (WPSH), in contrast to patterns D4 and D5 in the bottom-right with widespread negative anomalies at low latitudes and very weak eastward-located WPSH. Patterns A5 and B5 in the lower-left characterize pronounced deep troughs at middle-high latitudes and southward displaced WPSH, while patterns C1, D1 and D2 in the top-right present very weak and northward shifted WPSH influenced by activities of tropical cyclones. Among the patterns in the lower-left portion, patterns A3, A4, B3 are characterized by East Asia-Pacific (EAP) teleconnection at positive phase and double blockings at high latitudes. In contrast, patterns C2, D3 and D4 on the right half of SOM feature the northward displaced WPSH or the negative phase of EAP teleconnection. Other intermediate CPs sharing similarities to the above-mentioned CPs such as the EAP-like patterns (B4, C3, C4 and C5) and northward-extended WPSH patterns (B1 and B2) are also identified (figure S1).

With different configurations of the intensity and positioning of synoptic systems, the 20 CPs produce diverse precipitation pattern over eastern China. Some CPs, which are assigned to distinct attributes, produce an opposite precipitation response for the south and north regions (figure S3). Among these CPs, patterns A3, A4 and B3 favors SFND, while patterns C2, D3 and D4 tend to produce precipitation pattern opposite to SFND. Changes in occurrence of these CPs will also bring a correspondingly north–south converse pattern of dynamic contribution (figures 1(a) and (c)). However, the dynamic effect induced by changes in the frequency of these CPs contributes positively both to the wetting in the south and drying in the north. This implies that the three CPs facilitating SFND are occurring more often and that concurrently the three CPs unfavorable to SFND are decreasing in frequency (also corroborated in figure 2). Noteworthily, amongst the CPs contributing positively to both the south wetting and north drying, the above-mentioned six CPs (except pattern B3 for the north region) have provided the largest positive dynamic contributions (hatched bars in figures 1(a) and (c)). Of the total positive dynamic contribution to the south wetting and north drying, the six CPs account for 84% and 68% respectively. In addition, the wetting-drying contrasts between the south and north region dynamically caused by the frequency changes of these six CPs are the strongest,

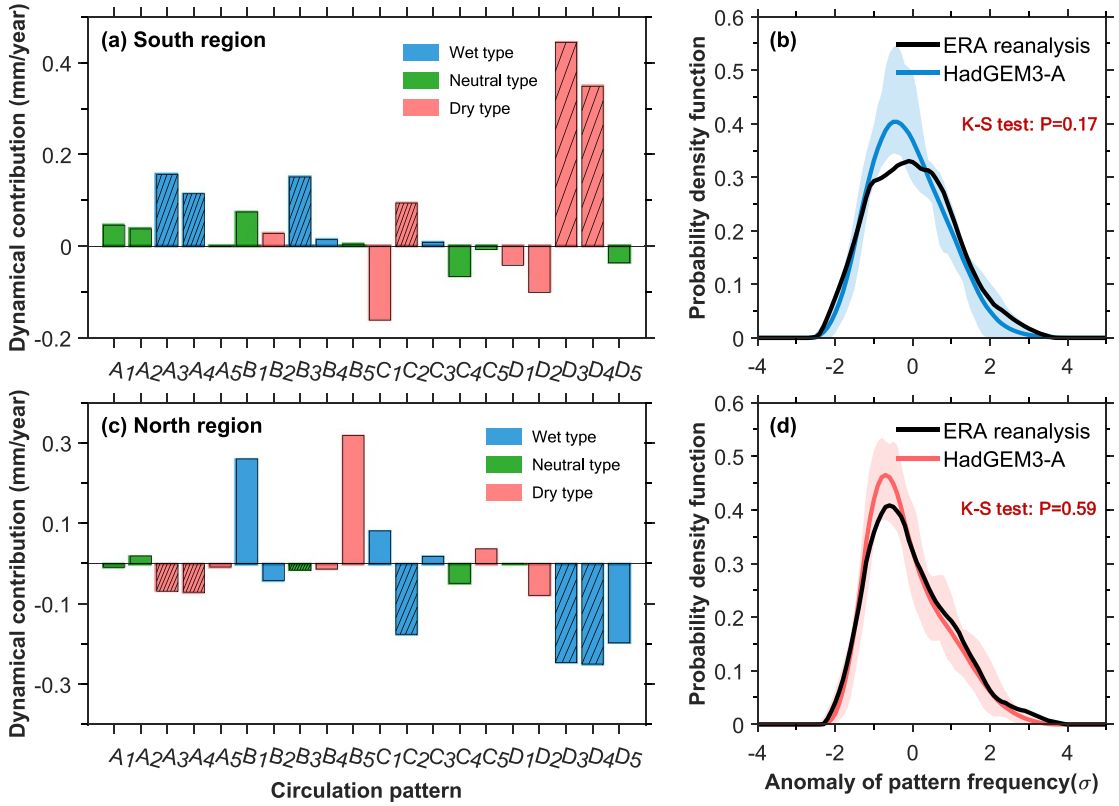

Figure 1. Dynamical contributions to the trends in domain-averaged summer total precipitation anomalies induced purely by the trends in occurrence of CPs during 1961–2013 in the (a) south and (c) north regions of eastern China affected by SFND, based on the clustering of CPs via ERA reanalysis. Hatched bars indicate the positive dynamic contributions from the six CPs (except pattern B3 for the north region) are the largest, amongst the CPs contributing positively to both the south wetting and north drying. The fitted PDFs for the standardized total frequency anomalies of patterns (b) A3, A4 and B3 and (d) C2, D3 and D4 during 1961–2013 in ERA reanalysis and ALL forcing simulations from HadGEM3-A-N216 (with reference to 1961–2010 climatology); shadings denote the full range of the ensemble.

compared to the other CPs (figure S4). In other word, the altering occurrences of these CPs create the most favorable dynamical conditions for SFND. Therefore, changes in these CPs play a key role in the contrasting precipitation trends over eastern China. Whether the frequency changes in these CPs are a manifestation of anthropogenic climate change is further explored.

Since the confidence of subsequent D&A analysis is contingent on the capabilities of the models employed, an evaluation of HadGEM3-A-N216's performance in simulating the occurrence of various CPs during 1961–2013 is performed. The PDFs for the frequency of the selected CPs constructed with ERA analysis and ALL forcing simulations over 1961–2013 show no visible difference (figures 1(b) and (d)). The two-sample Kolmogorov–Smirnov (K–S) test (Massey 1951, Wilks 2006) does not reject the null hypothesis that the frequency of the selected CPs favorable ($P = 0.17$) or unfavorable to SFND ($P = 0.59$) in the reanalysis and ALL forcing experiment come from populations with the same distribution. The interannual variability of the frequency of the selected CPs facilitating or counteracting SFND in ERA reanalysis is generally encompassed by the ensemble range of HadGEM3-A-N216 (figures 2(a) and (c)). For the ERA reanalysis, the standard deviations of the frequency of the selected CPs facilitating and counteracting SFND are 9.31 and 12.57 d, while for the ALL forcing multimember ensemble the median standard deviations are 8.38 and 11.8 d respectively. Overall, the interannual variabilities of the frequencies of the selected CPs from ALL forcing simulations resemble those in ERA reanalysis to a large extent. HadGEM3-A-N216 reproduces the trend in the occurrence of the CPs facilitating SFND reasonably well, but tends to slightly underestimate the negative trend of CPs counteracting SFND (figures 2(b) and (d)). For the PDFs and long-term change of each individual CP, HadGEM3-A-N216 also performs well for the most part (figures S5 and S6). These evidences demonstrate that HadGEM3-A-N216 is adequate for examining the trend in the frequency of CPs.

The occurrence of CPs facilitating SFND has increased by 1.55 and 1.87 d per 10 years (d 10 yr^{-1}), respectively, in ERA reanalysis and the ensemble mean of ALL forcing during 1961–2013, statistically significant at the 95% confidence level (figure 2(b)). In contrast, the ensemble mean of the NAT forcing simulations exhibits a weak negative trend in

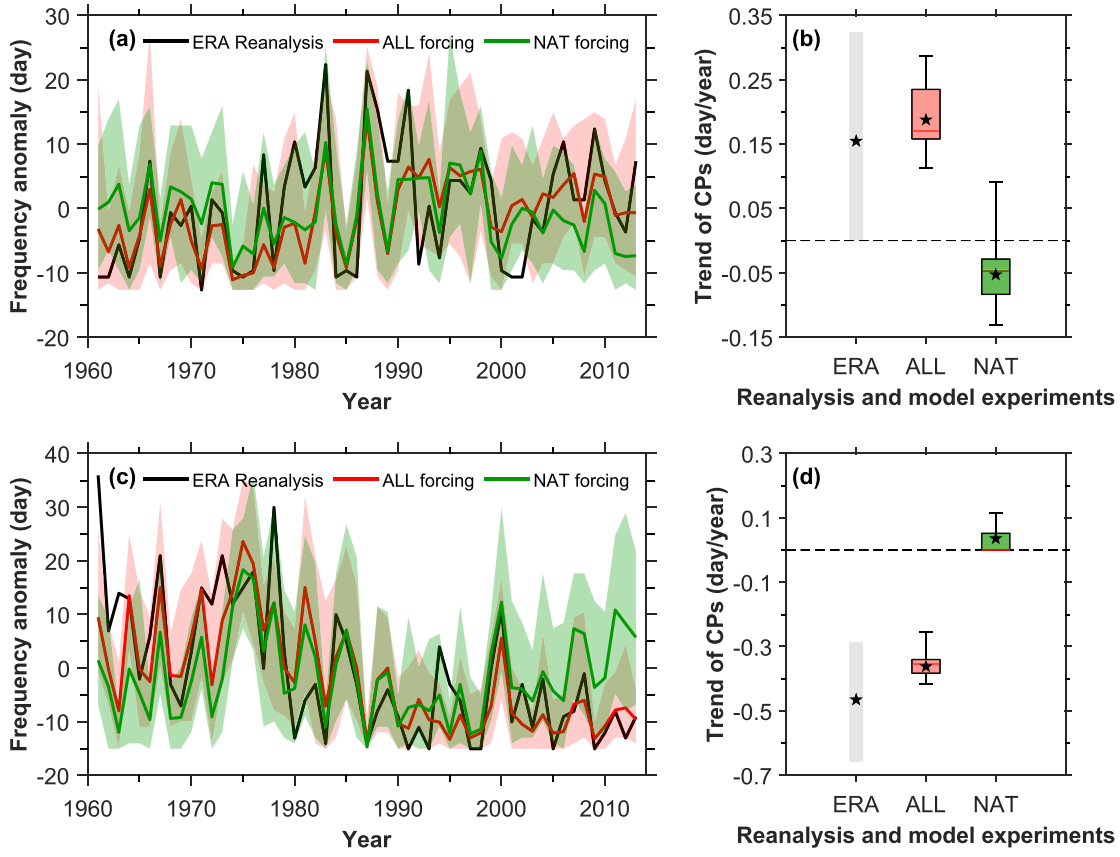

Figure 2. Time series of the total frequency anomalies for (a) the three CPs (A3, A4 and B3) facilitating SFND and (c) the three CPs (C2, D3 and D4) counteracting SFND during 1961–2013 (with reference to 1961–2010 climatology). Linear trends in the total frequency anomalies of (b) the three CPs facilitating SFND and (d) the three CPs counteracting SFND during 1961–2013 in ERA reanalysis (95% CI indicated by grey shadings), ALL and NAT forcing simulations from HadGEM3-A-N216. Horizontal bars of the box plots in (b) and (d) from bottom to up indicate the smallest, first quartile, median (red bar), third quartile, and largest values among ensemble members. Asterisks denote the trend in the total frequency anomalies of CPs from ERA reanalysis and the multimember ensemble mean.

the occurrence of CPs facilitating SFND. Similarly, compared with the significant negative trends in ERA reanalysis (-4.65 d 10 yr^{-1}) and the ensemble mean of ALL forcing (-3.62 d 10 yr^{-1}), trends in the CPs counteracting SFND from NAT forcing simulations are weak and of opposite sign (figure 2(d)). Although the interannual variability driven by only natural forcing generally keeps pace with that in ERA reanalysis and the ALL forcing experiment, the significant trends in frequency of the selected CPs would not occur without anthropogenic influence. This is also validated by the distribution shifts between the recent 20 year period of 1994–2013 and the earlier 20 year period of 1961–1980 in the model experiments with and without anthropogenic forcing (figure S7). Inconsistent with the shift of entire distributions in ERA reanalysis and the ALL forcing experiment to higher (lower) values for the CPs favorable (unfavorable) to SFND, distributions in the naturally forced experiment stay statistically unchanged at the 95% confidence level ($P > 0.05$ based on the K–S test). In short, the above evidences confirm that anthropogenic influence is clearly detectable in the long-term frequency changes of CPs favorable and unfavorable to SFND.

To address the probability change in the occurrence of CPs, the distribution shift from the counterfactual natural to the factual world in the recent 20 year period (1994–2013) is explored. Relative to the natural forcing experiment, PDFs of ALL forcing shift to the positive and negative sides, respectively, for CPs favorable or unfavorable to SFND (figures 3(a) and (c)). This signifies that anthropogenic influence has increased the probability of favorable CPs (figure 3(a)) but decreased the likelihood of unfavorable CPs (figure 3(c)). Quantitatively speaking, for the 90th percentile threshold defined from the NAT experiment (one-in-ten year event), the occurrence of CPs facilitating SFND has increased about twofold (RR = 1.89, 95% confidence interval (CI): 1.30–2.81) while CPs counteracting SFND have become 7.75 times less frequent due to anthropogenic influence (RR = 0.129, 95% CI: 0.026–0.28). Human influence has shortened the return period of the CPs facilitating SFND at the natural 90th-percentile

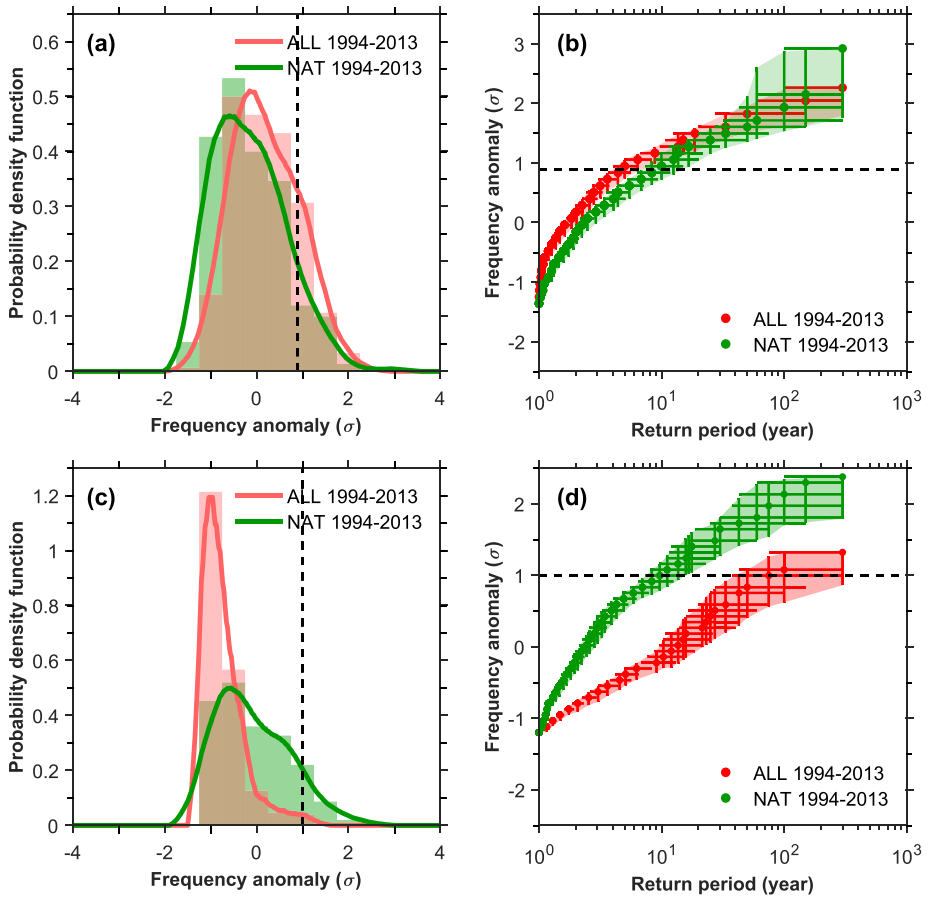

Figure 3. Histograms (bars) and fitted PDFs (lines) for the standardized total frequency anomalies of (a) the three CPs facilitating SFND and (c) the three CPs counteracting SFND during 1994–2013 in ALL and NAT forcing simulations from HadGEM3-A-N216 (with reference to 1961–2010 climatology). Return periods for the standardized total frequency anomalies of (b) the three CPs facilitating SFND and (d) the three CPs counteracting SFND in ALL and NAT forcing ensembles. Each marker represents a sample. The vertical and horizontal errors bars indicate the 95% CI of frequency anomalies and return periods. The black dashed line indicates the 90th percentile threshold defined from the NAT experiment during 1994–2013.

threshold to 4.41 years (CI: 3.57–5.61; figure 3(b)). In contrast, the return period of the CPs counteracting SFND which occur once a decade in the natural world has been lengthened to 75 years (CI: 37.5–300; figure 3(d)). Thus, from a probabilistic perspective, anthropogenic influence has played a critical role in increasing the likelihood of CPs facilitating SFND while decreasing that of CPs unfavorable to SFND.

A least-squares multiple linear regression analysis is performed to explore the link between the frequency of CPs and summer precipitation for each station. The frequencies of all the 20 CPs except patterns A1 and A2 are used as predictors. Due to the invariant total frequencies of the 20 CPs (92 d in summer), the frequency of each CP is fully correlated with the total frequencies of the remaining CPs. Furthermore, the weak dynamic contributions caused by the frequency changes in patterns A1 and A2 for both the north and south region indicate a weak link between SFND and patterns A1 and A2 (figures 1(a) and (c)). To avoid multicollinearity caused by repetitive information from predictors whilst minimizing the loss of information, the frequency of patterns A1 and A2 are eliminated from the predictors.

The reconstructed trends using CP frequencies from ERA reanalysis and the ALL forcing experiment give a good representation of the converse north–south precipitation trends over eastern China during 1961–2013 (figures 4(a) and S8(a), S8(c), S8(d)). The underestimation of strong positive trends and overestimation of several negative trends from ALL forcing indicate that other processes such as thermodynamics could also be at play (figures 4(a) and (b)). Despite this, changes in CP occurrences could explain a large part of the trends in precipitation over eastern China during 1961–2013. In comparison, the precipitation regressed from naturally forced CP frequencies is characterized by very weak trends centered around zero (figures 4(a) and S8(b)). The single-peak PDF of precipitation trends reconstructed from the NAT forcing experiment is statistically distinguishable from other two-peak PDFs of observed and regressed precipitation trends via ERA reanalysis and the ALL forcing experiment ($P < 0.05$, based on the K–S test; figure 4(b)). The mismatch in precipitation trends reconstructed from CP frequencies with and without anthropogenic forcing has two main implications. First, the occurrence of CPs

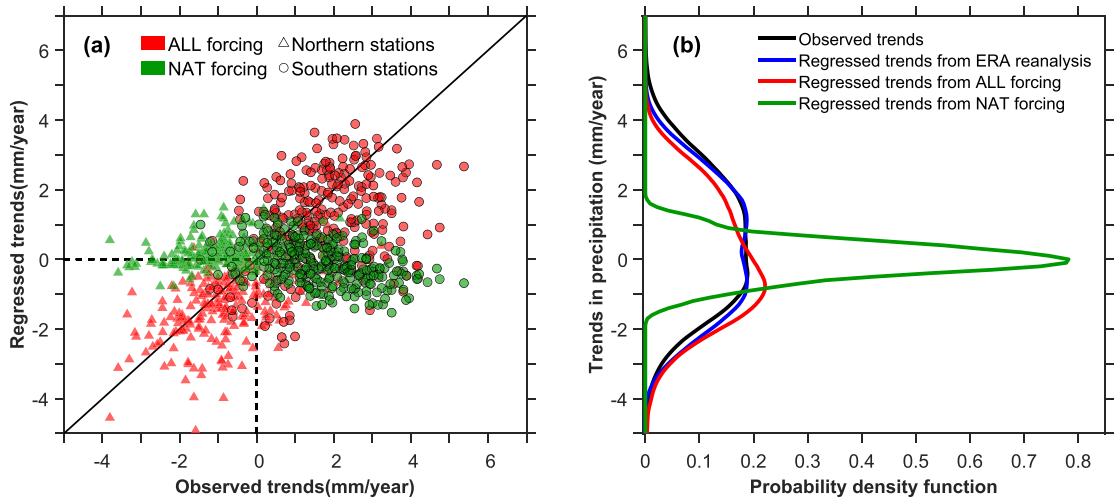

Figure 4. (a) Scatter plot for summer precipitation trends regressed with the ensemble mean frequency of all the 20 CPs except A1 and A2 in ALL and NAT forcing simulations from HadGEM3-A-N216 against the observed trends at all stations in eastern China during 1961–2013. (b) PDFs for the observed and linear regressed trends from the frequency of CPs in ERA reanalysis and the ensemble mean of ALL and NAT forcing simulations from HadGEM3-A-N216 for summer precipitation at all stations in eastern China during 1961–2013.

in the factual world driven by ALL forcing is different from that in the counterfactual natural world, which further confirms anthropogenic influence on the changing prevalence of the clustered CPs. Second, the north–south dipole pattern was evident when considering CP frequencies from the ALL forcing experiment, but not from CPs frequencies driven by purely natural forcing. Thus, anthropogenic forcing has played a critical role in the contrasting north–south precipitation trends over eastern China during 1961–2013.

4. Concluding remarks

Changes in the occurrence of CPs associated with precipitation anomalies characterized by either SFND or the opposite pattern reveal a large part of the positive dynamic contribution to the wetting in the south and drying in the north over eastern China during 1961–2013. Both the trends and long-term distribution shift in the frequency of these CPs in ERA reanalysis are generally consistent with the model experiments that include anthropogenic forcing, but are inconsistent with the naturally forced experiments. This demonstrates that the increasing trend in CPs favoring SFND and the decreasing trend in CPs disfavoring SFND are attributable to human influence. From the perspective of probabilistic event attribution, anthropogenic influence has increased the likelihood of the occurrence of CPs facilitating SFND, but decreased that of CPs unfavorable to SFND.

The regression analysis shows that CP frequencies driven by both anthropogenic and natural forcing succeed in reproducing the dipole pattern of precipitation trends over eastern China during 1961–2013. In contrast, the precipitation trends reconstructed from naturally forced CP frequencies alone appear to be very weak and unable to capture the north–south contrast. The difference between the reconstructed precipitation trends not only confirms the differential responses of CPs to forcing with and without human influence, but also signifies the critical role of human influence in shaping the contrasting north–south precipitation trends over eastern China during 1961–2013.

Data availability statement

The data that support the findings of this study are openly available. The links are listed below. Observed precipitation data is available at www.nmic.cn/site/index.html. ERA-Interim and ERA-40 reanalyses are available at https://apps.ecmwf.int/datasets/, simulations with and without anthropogenic influence from HadGEM3-A-N216 at https://data.ceda.acuk/badc/eucleia/data/EUCLEIA/output/MOHC/HadGEM3-A-N216.

Acknowledgments

This study was jointly supported by the National Key R&D Program of China (2018YFC1507700), the National Natural Science Foundation of China (41905082) and the Basic Research to Operation Funds of the Chinese Academy of Meteorological Sciences (2019Y009). SFBT & FCL were funded by the UK–China Research & Innovation Partnership Fund through the Met Office Climate Science for Service Partnership (CSSP) China as part of the Newton Fund.

ORCID iDs

Baiquan Zhou https://orcid.org/0000-0002-3709-5336
Panmao Zhai https://orcid.org/0000-0002-1813-0159
Simon F B Tett https://orcid.org/0000-0001-7526-560X
Fraser C Lott https://orcid.org/0000-0001-5184-4156

References

Bao M and Wallace J M 2015 Cluster analysis of northern hemisphere wintertime 500 hPa flow regimes during 1920–2014 *J. Atmos. Sci.* **72** 3597–608
Belleflamme A, Fettweis X, Lang C and Erpicum M 2013 Current and future atmospheric circulation at 500 hPa over Greenland simulated by the CMIP3 and CMIP5 global models *Clim. Dyn.* **41** 2061–80
Bindoff N L *et al* 2013 Detection and attribution of climate change: from global to regional *Climate Change 2013: The Physical Science Basis. Contribution of Working Group I to the Fifth Assessment Report of the Intergovernmental Panel on Climate Change* ed T F Stocker, D Qin, G-K Plattner, M Tignor, S K Allen, J Boschung, A Nauels, Y Xia, V Bex and P M Midgley (Cambridge: Cambridge University Press) pp 86
Boé J and Terray L 2008 A weather-type approach to analyzing winter precipitation in France: twentieth-century trends and the role of anthropogenic forcing *J. Clim.* **21** 3118–33
Burke C and Stott P 2017 Impact of anthropogenic climate change on the East Asian summer monsoon *J. Clim.* **30** 5205–20
Cattiaux J, Douville H and Peings Y 2013 European temperatures in CMIP5: origins of present-day biases and future uncertainties *Clim. Dyn.* **41** 2889–907
Christidis N, Stott P A, Scaife A A, Arribas A, Jones G S, Copsey D, Knight J R and Tennant W J 2013 A new HADGEM3-a-based system for attribution of weather- and climate-related extreme events *J. Clim.* **26** 2756–83
Ciavarella A, Christidis N, Andrews M, Groenendijk M, Rostron J, Elkington M, Burke C, Lott F C and Stott P A 2018 Upgrade of the HadGEM3-A based attribution system to high resolution and a new validation framework for probabilistic event attribution *Weather Clim. Extrem.* **20** 9–32
Corti S, Molteni F and Palmer T N 1999 Signature of recent climate change in frequencies of natural atmospheric circulation regimes *Nature* **398** 799–802
Day J A, Fung I and Liu W 2018 Changing character of rainfall in eastern China, 1951–2007 *Proc. Natl Acad. Sci. USA* **115** 2016–21
Dee D P *et al* 2011 The ERA-Interim reanalysis: configuration and performance of the data assimilation system *Q. J. R. Meteorol. Soc.* **137** 553–97
Ding Y, Wang Z and Sun Y 2008 Inter-decadal variation of the summer precipitation in East China and its association with decreasing Asian summer monsoon. Part I: observed evidences *Int. J. Climatol.* **28** 1139–61
Dong B, Wilcox L J, Highwood E J and Sutton R T 2019 Impacts of recent decadal changes in Asian aerosols on the East Asian summer monsoon: roles of aerosol–radiation and aerosol–cloud interactions *Clim. Dyn.* **53** 3235–56
Efron B and Tibshirani R J 1998 *An Introduction to the Bootstrap* (New York: Chapman and Hall)
Fabiano F, Christensen H M, Strommen K, Athanasiadis P, Baker A, Schiemann R and Corti S 2020 Euro-Atlantic weather regimes in the PRIMAVERA coupled climate simulations: impact of resolution and mean state biases on model performance *Clim. Dyn.* **54** 5031–48
Field C B *et al* 2012 *Managing the Risks of Extreme Events and Disasters to Advance Climate Change Adaptation* (Cambridge: Cambridge University Press) pp 582
Fischer E M, Beyerle U and Knutti R 2013 Robust spatially aggregated projections of climate extremes *Nat. Clim. Change* **3** 1033–8
Hao X, He S, Wang H and Han T 2019 Quantifying the contribution of anthropogenic influence to the East Asian winter monsoon in 1960–2012 *Atmos. Chem. Phys.* **19** 9903–11
He J and Soden B J 2016 Does the lack of coupling in SST-forced atmosphere-only models limit their usefulness for climate change studies? *J. Clim.* **29** 4317–25
Hegerl G and Zwiers F 2011 Use of models in detection and attribution of climate change *Wiley Interdiscip. Rev. Clim. Change* **2** 570–91
Hersbach H, Rosnay P, Bell B, Schepers D and Al E 2018 Operational global reanalysis: progress, future directions and synergies with NWP *ERA Rep. Ser.* **27** 1–63
Hewitson B C and Crane R G 2002 Self-organizing maps: applications to synoptic climatology *Clim. Res.* **22** 13–26
Horton D E, Johnson N C, Singh D, Swain D L, Rajaratnam B and Diffenbaugh N S 2015 Contribution of changes in atmospheric circulation patterns to extreme temperature trends *Nature* **522** 465–9
Huang R H, Liu Y and Feng T 2013 Interdecadal change of summer precipitation over Eastern China around the late-1990s and associated circulation anomalies, internal dynamical causes *Chinese Sci. Bull.* **58** 1339–49
Huguenin M F, Fischer E M, Kotlarski S, Scherrer S C, Schwierz C and Knutti R 2020 Lack of change in the projected frequency and persistence of atmospheric circulation types over central Europe *Geophys. Res. Lett.* **47** e2019GL086132
Huth R 2000 A circulation classification scheme applicable in GCM studies *Theor. Appl. Climatol.* **67** 1–18
Jiang N, Luo K, Beggs P J, Cheung K and Scorgie Y 2015 Insights into the implementation of synoptic weather-type classification using self-organizing maps: an Australian case study *Int. J. Climatol.* **35** 3471–85
Jiang Z, Huo F, Ma H, Song J and Dai A 2017 Impact of Chinese urbanization and aerosol emissions on the East Asian summer monsoon *J. Clim.* **30** 1019–39
Johnson S J *et al* 2016 The resolution sensitivity of the South Asian monsoon and Indo-Pacific in a global 0.35° AGCM *Clim. Dyn.* **46** 807–31
Kohonen T 2001 *Self-Organizing Maps* 3rd edn (New York: Springer) pp 501
Lennard C and Hegerl G 2015 Relating changes in synoptic circulation to the surface rainfall response using self-organising maps *Clim. Dyn.* **44** 861–79
Li C *et al* 2018 Attribution of extreme precipitation in the lower reaches of the Yangtze River during May 2016 *Environ. Res. Lett.* **13** 014015
Li X and Lu R 2017 Extratropical factors affecting the variability in summer precipitation over the Yangtze River Basin, China *J. Clim.* **30** 8357–74
Li X and Ting M 2017 Understanding the Asian summer monsoon response to greenhouse warming: the relative roles of direct radiative forcing and sea surface temperature change *Clim. Dyn.* **49** 2863–80
Li X, Ting M, Li C and Henderson N 2015 Mechanisms of Asian summer monsoon changes in response to anthropogenic forcing in CMIP5 models *J. Clim.* **28** 4107–25
Liu R, Liu S-C, Ralph J C, Shiu C-J, Li J, Wang J and Zhang Y 2015 Trends of extreme precipitation in Eastern China and their possible causes *Adv. Atmos. Sci.* **32** 1027–37
Lu C, Lott F C, Sun Y, Stott P A and Christidis N 2020 Detectable anthropogenic influence on changes in summer precipitation in China *J. Clim.* **33** 5357–69
Ma S *et al* 2017 Detectable anthropogenic shift toward heavy precipitation over eastern China *J. Clim.* **30** 1381–96

Marvel K and Bonfils C 2013 Identifying external influences on global precipitation *Proc. Natl Acad. Sci. USA* **110** 19301–6

Massey F J 1951 The Kolmogorov-Smirnov test for goodness of fit *J. Am. Stat. Assoc.* **46** 68–78

Min S K, Zhang X and Zwiers F 2008 Human-induced Arctic moistening *Science* **320** 518–20

Nigam S, Zhao Y, Ruiz-Barradas A and Zhou T 2016 The South-Flood North-Drought pattern over eastern china and the drying of the gangetic plain *Climate change: Multidecadal and beyond* (Singapore: World Scientific) pp 23

Pfahl S, O'Gorman P A and Fischer E M 2017 Understanding the regional pattern of projected future changes in extreme precipitation *Nat. Clim. Change* **7** 423–7

Qian C and Zhou T 2014 Multidecadal variability of North China aridity and its relationship to PDO during 1900–2010 *J. Clim.* **27** 1210–22

Rayner N A, Parker D E, Horton E B, Folland C K, Alexander L V, Rowell D P, Kent E C and Kaplan A 2003 Global analyses of sea surface temperature, sea ice, and night marine air temperature since the late nineteenth century *J. Geophys. Res. Atmos.* **108** 4407

Reusch D B, Alley R B and Hewitson B C 2005 Relative performance of self-organizing maps and principal component analysis in pattern extraction from synthetic climatological data *Polar Geogr.* **29** 188–212

Reusch D B, Alley R B and Hewitson B C 2007 North Atlantic climate variability from a self-organizing map perspective *J. Geophys. Res. Atmos.* **112** 1–20

Rousi E, Sslten F, Rahmstorf S and Coumou D 2021 Changes in north Atlantic atmospheric circulation in a warmer climate favor winter flooding and summer drought over europe *J. Clim.* **34** 2277–95

Sarojini B B, Stott P A and Black E 2016 Detection and attribution of human influence on regional precipitation *Nat. Clim. Change* **6** 669–75

Schaller N *et al* 2016 Human influence on climate in the 2014 southern England winter floods and their impacts *Nat. Clim. Change* **6** 627–34

Shepherd T G 2014 Atmospheric circulation as a source of uncertainty in climate change projections *Nat. Geosci.* **7** 703–8

Song F, Zhou T and Qian Y 2014 Responses of East Asian summer monsoon to natural and anthropogenic forcings in the 17 latest CMIP5 models *Geophys. Res. Lett.* **41** 596–603

Stott P A *et al* 2016 Attribution of extreme weather and climate-related events *Wiley Interdiscip. Rev. Clim. Change* **7** 23–41

Stott P A, Gillett N P, Hegerl G C, Karoly D J, Stone D A, Zhang X and Zwiers F 2010 Detection and attribution of climate change: a regional perspective *Wiley Interdiscip. Rev. Clim. Change* **1** 192–211

Taylor K E, Stouffer R J and Meehl G A 2012 An overview of CMIP5 and the experiment design *Bull. Am. Meteorol. Soc.* **93** 485–98

Tian F, Dong B, Robson J and Sutton R 2018 Forced decadal changes in the East Asian summer monsoon: the roles of greenhouse gases and anthropogenic aerosols *Clim. Dyn.* **51** 3699–715

Tymvios F, Savvidou K and Michaelides S C 2010 Association of geopotential height patterns with heavy rainfall events in Cyprus *Adv. Geosci.* **23** 73–78

Uppala S M *et al* 2005 The ERA-40 re-analysis *Q. J. R. Meteorol. Soc.* **131** 2961–3012

Vautard R *et al* 2019 Evaluation of the HadGEM3-A simulations in view of detection and attribution of human influence on extreme events in Europe *Clim. Dyn.* **52** 1187–210

Vautard R, Yiou P, Otto F, Stott P, Christidis N, Van Oldenborgh G J and Schaller N 2016 Attribution of human-induced dynamical and thermodynamical contributions in extreme weather events *Environ. Res. Lett.* **11** 114009

Wang T, Wang H J, Otterå O H, Gao Y Q, Suo L L, Furevik T and Yu L 2013 Anthropogenic agent implicated as a prime driver of shift in precipitation in eastern China in the late 1970s *Atmos. Chem. Phys.* **13** 12433–50

Wilks D S 2006 *Statistical Methods in the Atmospheric Sciences* (*International Geophysics Series* vol 91) (Amsterdam: Elsevier Academic) pp 627

Yang Q, Ma Z, Fan X, Yang Z L, Xu Z and Wu P 2017 Decadal modulation of precipitation patterns over eastern China by sea surface temperature anomalies *J. Clim.* **30** 7017–33

Zhang R 2015 Changes in East Asian summer monsoon and summer rainfall over eastern China during recent decades *Sci. Bull.* **60** 1222–4

Zhang X, Zwiers F W, Hegerl G C, Lambert F H, Gillett N P, Solomon S, Stott P A and Nozawa T 2007 Detection of human influence on twentieth-century precipitation trends *Nature* **448** 461–5

Zhou B, Zhai P and Chen Y 2020a Contribution of changes in synoptic-scale circulation patterns to the past summer precipitation regime shift in Eastern China *Geophys. Res. Lett.* **47** e2020GL087728

Zhou T *et al* 2020b The dynamic and thermodynamic processes dominating the reduction of global land monsoon precipitation driven by anthropogenic aerosols emission *Sci. Chin. Earth Sci.* **63** 919–33

Zhou T, Gong D, Li J and Li B 2009 Detecting and understanding the multi-decadal variability of the East Asian Summer Monsoon—recent progress and state of affairs *Meteorol. Zeitschrift* **18** 455–67

Zhou T, Song F, Ha K J and Chen X 2017 Decadal Change of East Asian Summer Monsoon: Contributions of Internal Variability and External Forcing *The Global Monsoon System: Research and Forecast* (Singapore: World Scientific) pp 10